MNRAS **000**, 1–16 (2016) Preprint 5 April 2024 Compiled using MNRAS LATEX style file v3.0

Constraining the Mass–Richness Relationship of redMaPPer Clusters with Angular Clustering

Eric J. Baxter,[1⋆] Eduardo Rozo,[2] Bhuvnesh Jain,[1] Eli Rykoff,[3,4] Risa H. Wechsler[3,4]
[1] *Center for Particle Cosmology, Department of Physics, University of Pennsylvania, Philadelphia, PA 19104*
[2] *Department of Physics, University of Arizona, Tucson, AZ 85721, USA*
[3] *Kavli Institute for Particle Astrophysics and Cosmology, Department of Physics, Stanford University, Stanford, CA, 94305*
[4] *SLAC National Accelerator Laboratory, Menlo Park, CA, 94025*

Last updated 5 April 2024

ABSTRACT

The potential of using cluster clustering for calibrating the mass-observable relation of galaxy clusters has been recognized theoretically for over a decade. Here, we demonstrate the feasibility of this technique to achieve high precision mass calibration using redMaPPer clusters in the Sloan Digital Sky Survey North Galactic Cap. By including cross-correlations between several richness bins in our analysis we significantly improve the statistical precision of our mass constraints. The amplitude of the mass–richness relation is constrained to 7% statistical precision. However, the error budget is systematics dominated, reaching an 18% total error that is dominated by theoretical uncertainty in the bias–mass relation for dark matter halos. We perform a detailed treatment of the effects of assembly bias on our analysis, finding that the contribution of such effects to our parameter uncertainties is somewhat greater than that of measurement noise. We confirm the results from Miyatake et al. (2015) that the clustering amplitude of redMaPPer clusters depends on galaxy concentration, and provide additional evidence in support of this effect being due to some form of assembly bias. The results presented here demonstrate the power of cluster clustering for mass calibration and cosmology provided the current theoretical systematics can be ameliorated.

Key words: cosmology: observations – large-scale structure of Universe – methods: analytical

1 INTRODUCTION

The abundance of galaxy clusters is a powerful probe of cosmology (Weinberg et al. 2013). The observed number density of clusters as a function of redshift, $n(z)$, is sensitive to both the expansion history of the Universe and to the growth of structure. This dual sensitivity enables cluster abundance measurements to distinguish between dark energy models and modified gravity (Huterer et al. 2013). However, modeling the cluster abundance to extract cosmological constraints is challenging because the abundance depends sensitively on the masses of the observed clusters. Because clusters live at the extreme tails of the mass function where the abundance is falling exponentially, small changes in the cluster mass can have a large impact on the predicted cluster abundance. Moreover, measuring cluster masses is difficult because it requires relating observable quantities to cluster mass. The mass–observable relationships are often noisy and subject to large systematic uncertainties (Rozo et al. 2014; Sereno & Ettori 2015). For these reasons, the dominant systematic currently affecting cosmological constraints derived from cluster abundance measurements is uncertainty in cluster masses (Vikhlinin et al. 2009; Rozo et al. 2010; Sehgal et al. 2011; Benson et al. 2013; Mantz et al. 2015; Planck Collaboration et al. 2015a). If these mass uncertainties can be reduced, the full power of cluster abundance measurements can be exploited, and clusters will become highly competitive probes of dark energy and modified gravity (Albrecht et al. 2006).

The spatial clustering of galaxy clusters is sensitive to cluster mass, with higher mass clusters being more strongly clustered on the sky. To quantify the degree of clustering it is common to define the *bias* as the square root of the ratio of the correlation function of clusters — which we identify with massive dark matter halos — to that of all matter. The relationship between halo bias and halo mass, $b(M)$, is well understood via the halo model (for a review see Cooray & Sheth 2002) and can be calibrated from simulations (e.g. Tinker et al. 2010). Several authors have highlighted the possibility of using measure-

⋆ E-mail: ebax@sas.upenn.edu

ments of the clustering biases of clusters to do a "self-calibrated" cluster cosmology analysis, i.e. to jointly fit for cosmological parameters as well as parameters governing the relationship between observable quantities and cluster mass (e.g. Majumdar & Mohr 2003; Lima & Hu 2004; Hu & Cohn 2006; Holder 2006).

In this work, we perform the first half of the self-calibration program, i.e. measuring the clustering biases of a catalog of optically detected galaxy clusters and using the measured biases to constrain the mass–observable relationship. To this end, we use the catalog of redMaPPer clusters (Rykoff et al. 2014) identified in the Sloan Digital Sky Survey (SDSS). The relevant observable for the redMaPPer clusters is the *richness*, a measure of the number of galaxies within the cluster. Using the measured correlation functions and the predicted $b(M)$, we calibrate the mass–richness relation for the redMaPPer clusters.

Two of the most significant challenges for using cluster clustering to calibrate cluster masses are line-of-sight cluster projections and assembly bias. Chance alignment of clusters along the line of sight can alter the richness estimates of these clusters and change the measured clustering amplitude. If this effect is not accounted for, constraints on the mass–richness relation of the redMaPPer clusters could be biased. Assembly bias refers to the dependence of halo clustering on assembly history or other quantities in addition to halo mass (Gao et al. 2005; Wechsler et al. 2006; Jing et al. 2007; Dalal et al. 2008). Recently, Miyatake et al. (2015) have measured dependence of the clustering of redMaPPer clusters on $\overline{R}_{\rm mem}$, the average radial separation between the cluster center and its member galaxies. Dependence of the clustering amplitude on $\overline{R}_{\rm mem}$ (or any other properties of the halo beyond the halo mass dependence) complicates any attempt to extract constraints on the mass–richness relation or cosmology using $b(M)$. Below, we develop methodology to account for the effects of both cluster projections and assembly bias on our constraints on the parameters of the mass–richness relationship.

The outline of the paper is as follows: we introduce the formalism for describing the correlation function measurements in §2; the cluster catalog is described in §3; the measurement of the correlation function and its covariance are described in §4; our model for the correlation function and fitting procedure — including our treatment of projection and assembly bias effects — are described in §5; results are presented in §6; we explore the various contributions to our error budget in §7; the cosmology dependence of our constraints is considered in §8; finally, our conclusions are given in §9.

Throughout, all cluster masses refer to M_{200m}, i.e. the mass enclosed within a sphere centered on a cluster such that the mean density within that sphere is 200 times the mean density of the Universe at the cluster's redshift. Our fiducial analysis assumes the best-fit flat ΛCDM model from an analysis of cosmic microwave background data and other data sets by Planck Collaboration et al. (2015b). The cosmological parameters in this model are $\Omega_m = 0.309$, $h_0 = H_0/(100{\rm km/s/Mpc}) = 0.677$, $\Omega_b = 0.0486$, $\tau = 0.066$, $n_s = 0.9667$ and $A_s = 2.14 \times 10^{-9}$ at a pivot scale of $k = 0.05\,{\rm Mpc}^{-1}$. In §8 we explore how our parameter constraints are affected by variations in the assumed cosmological model.

2 FORMALISM

We define $n(\hat{\phi})$ to be the projected density of clusters in the direction specified by the unit vector $\hat{\phi}$. The overdensity in the same direction is then defined as

$$\delta(\hat{\phi}) \equiv \frac{n(\hat{\phi}) - \bar{n}(\hat{\phi})}{\bar{n}(\hat{\phi})}, \tag{1}$$

where $\bar{n}(\hat{\phi})$ is the average of $n(\hat{\phi})$ over all $\hat{\phi}$. The clustering of clusters on the sky can be characterized in terms of the angular correlation function, $w(\theta)$:

$$w(\theta) = \langle \delta(\hat{\phi})\delta(\hat{\phi}')\rangle, \tag{2}$$

where the average is taken over all possible $\hat{\phi}$ and $\hat{\phi}'$ such that the angular separation between $\hat{\phi}$ and $\hat{\phi}'$ is θ.

We measure the angular correlation function of the redMaPPer clusters in bins of richness and redshift; in addition, we also measure several cross-bin angular correlations. To keep the notation simple, we use a single Greek superscript to represent both the richness and redshift bins. The correlation function between richness/redshift bin α and richness/redshift bin β will be denoted with $w^{\alpha\beta}(\theta)$. Occasionally we suppress the superscripts on $w(\theta)$ for notational convenience.

The correlation function $w^{\alpha\beta}(\theta)$ is related to the angular power spectrum, $C_\ell^{\alpha\beta}$, by

$$w^{\alpha\beta}(\theta) = \sum_{l=0}^{\infty} \left(\frac{2l+1}{4\pi}\right) P_\ell(\cos\theta) C_\ell^{\alpha\beta}, \tag{3}$$

where P_ℓ is the Legendre polynomial of order ℓ. We can relate $C_\ell^{\alpha\beta}$ for redMaPPer clusters to the matter power spectrum using the Limber approximation:

$$C_\ell^{\alpha\beta} = \int dz\; W^\alpha(z) W^\beta(z) \frac{H(z)}{d_A^2(z)} b^2(k,z) P\left(k = \frac{\ell+1/2}{\chi(z)}; z\right), \tag{4}$$

where $H(z)$ is the Hubble parameter at redshift z, $d_A(z)$ is the angular diameter distance, $\chi(z)$ is the comoving distance, and we have assumed a spatially flat Universe (Limber 1953). The weight function $W^\alpha(z)$ is the distribution of clusters in the α-th richness/redshift bin as a function of redshift, normalized such that $\int dz\, W^\alpha(z) = 1$. The $b(z,k)$ term is the bias of the redMaPPer clusters, which we discuss in more detail below. The Limber approximation is expected to be valid when the redshift selection function, $W^\alpha(z)$, is much wider than the scales of interest. In our case, the maximum scale that we probe is $\sim 25\,$Mpc, while the width of the selection function is $\sim 280\,$Mpc. We are therefore safely in the regime for which the Limber approximation should hold.

At large scales, the bias is expected to be independent of k. This is the so-called linear bias regime. At small scales, the bias may become scale-dependent and is difficult to model. We therefore restrict our analysis to the linear bias regime (but still at scales small enough that the Limber approximation holds). In this limit, the angular correlation function is simply

$$w^{\alpha\beta}(\theta) = b^\alpha b^\beta w_M^{\alpha\beta}(\theta), \tag{5}$$

where $w_M^{\alpha\beta}$ is the matter-matter correlation function, given by Eqs. 3 and 4 with $b(k,z) = 1$. The coefficients b^α and b^β are the linear bias parameters for the two richness/redshift

bins α and β; constraining these parameters for the redMaPPer clusters is one of the main goals of this analysis. The bias parameters should be thought of as averages across all clusters in a given richness/redshift bin.

3 DATA

Our analysis uses the redMaPPer (Rykoff et al. 2014) catalog of clusters identified in the SDSS (SDSS: York et al. 2000) 8^{th} Data Release (DR8 Aihara et al. 2011). The SDSS DR8 photometric galaxy catalog includes roughly $14,000$ deg^2 of imaging, which was reduced to $\sim 10,000$ deg^2 of high quality contiguous imaging for the purposes of cluster finding using the Baryon Oscillation Spectroscopic Survey (BOSS) mask (Dawson et al. 2013). Given a cluster candidate, redMaPPer uses the SDSS 5-band imaging to estimate the probability of any given galaxy in the field of being a red-sequence cluster member of the candidate cluster. The cluster richness is the total number of red-sequence members λ, and serves as our observable mass proxy. A detailed explanation of the redMaPPer algorithm can be found in Rykoff et al. (2014).

For the main results of this work we restrict our analysis to redMaPPer clusters identified in the North Galactic Cap (NGC) of SDSS, a contiguous region of $\sim 7,000$ deg^2 in the northern hemisphere. We restrict our analysis to the NGC for two reasons. First, the weak lensing mass calibration of redMaPPer clusters performed by Simet et al. (2016) (hereafter S16) is restricted to the NGC (for reasons discussed therein) and imposing the same restriction on our analysis makes comparison between the two works more straightforward. Second, as we discuss in §7.5, we find some tension between the clustering measurements in the NGC and the Southern Galactic Cap (SGC). We refrain from combining the parameter constraints derived from the NGC and SGC because of this tension, and only present results from the NGC because it represents a larger area than the SGC.

Our analysis relies on the redMaPPer v5.10 catalog,[1] an updated version of the original redMaPPer cluster catalog with a variety of modest improvements. Typical photometric redshift uncertainties are $\sigma_z/(1+z) \lesssim 0.01$, with photo$z$ biases controlled at the $\Delta z \approx 0.003$ level. This level of photometric redshift performance is sufficiently high that photometric redshift errors can be safely ignored in our analysis.

We note that while the redMaPPer v5.10 cluster catalog is publicly available, our analysis relies on a proprietary version of the catalog that extends the low richness threshold from $\lambda \geq 20$ to $\lambda \geq 5$. As discussed in Rykoff et al. (2014), the $\lambda \geq 20$ threshold is a purposely conservative selection that ensures a clean connection between individual dark matter halos and galaxy clusters selected by redMaPPer. We demonstrate below why our specific science goal allows us to use low richness clusters, even if the connection between halos and galaxy clusters is less secure for these low richness systems.

We restrict the catalog used in this work to clusters with $0.18 < z < 0.33$. The cut at the high redshift end ensures that the cluster catalog is volume limited (Rykoff et al. 2014). The cut at the low redshift end is chosen to maximize our signal to noise while ensuring that we remain in the linear bias regime (see discussion in §4).

4 CORRELATION FUNCTION MEASUREMENT

We measure $w^{\alpha\beta}(\theta)$ using the pair counting estimator of Landy & Szalay (1993). The Landy & Szalay (1993) estimator relies on computing three quantities to estimate the correlation function over a given angular bin: DD, RR, and DR. The quantity DD ('data-data') is the number of pairs of clusters that have an angular separation that is within the bin, RR ('random-random') is similarly defined for a catalog of points whose positions have been randomly and independently chosen on the sky, and DR ('data-random') is the number of cross pairs between the cluster and random catalogs. To reduce the effects of statistical noise, the random catalog is typically generated with ~ 30 to 50 times more points than the data catalog (although, more optimal estimators such as that of Baxter & Rozo (2013) can reduce this requirement).

For a particular angular bin, the Landy & Szalay (1993) estimate of the correlation function between richness/redshift bin α and richness/redshift bin β is

$$\hat{w}^{\alpha\beta} = \left(\frac{DD^{\alpha\beta}}{RR^{\alpha\beta}}\right)\left(\frac{R^\alpha R^\beta}{D^\alpha D^\beta}\right) - \left(\frac{DR^{\alpha\beta}}{RR^{\alpha\beta}}\right)\left(\frac{R^\alpha}{D^\alpha}\right) - \left(\frac{DR^{\beta\alpha}}{RR^{\alpha\beta}}\right)\left(\frac{R^\beta}{D^\beta}\right) + 1, \quad (6)$$

where D^α and R^α are the number of data and random points in the α richness/redshift bin, respectively (and similarly for D^β and R^β). The superscript notation indicates which bins are being correlated; $DD^{\alpha\beta}$, for instance, refers to the pair counts between bins α and β. All pair counting in our analysis is performed using the tree code `TreeCorr` [2] (Jarvis et al. 2004).

In order to account for survey geometry and selection effects, the random catalog used to compute DR and RR must be restricted to the same sky mask as the data. As the redMaPPer mask is richness and redshift dependent, the creation of an appropriate random catalog is non-trivial. The random catalog used in this work is generated as follows: for each cluster in the redMaPPer catalog, we select a random position in the sky, and test whether the cluster could have been detected at that location. If yes, the cluster is added to the random point catalog at this random location. If not, that cluster is rejected from the random catalog. Because of the large number of draws, every cluster is drawn multiple times, and we record the number of times the cluster was added to the random catalog (N_1), and the number of times the cluster was rejected (N_2). Every cluster is assigned a weight $W = (N_1 + N_2)/N_1$ in the random catalog to ensure that the weighted random points statistically reproduce the joint richness, redshift, and spatial distribution of the parent sample. We modify Eq. 6 so as to include these weights. Specifically, a random point with weight W_i contributes W_i

[1] `http://risa.stanford.edu/redmapper/`

[2] `https://github.com/rmjarvis/TreeCorr`

to R and DR, and two random points i and j contributes a weight $W_i W_j$ to RR.

Our baseline analysis uses $N_\theta = 4$ angular bins, $N_\lambda = 4$ richness bins and $N_z = 2$ redshift bins. We discuss the choice of angular bins in more detail in §4.1. The richness bin edges are $[5, 20, 28, 41, \infty)$, while the redshift bin edges are $[0.18, 0.26, 0.32]$. The bins have been chosen so that the measurement of $w^{\alpha\beta}(\theta)$ in each richness and redshift bin has roughly the same signal-to-noise.

In addition to measuring the angular auto-correlation functions of the clusters in each richness and redshift bin, we also measure the angular cross-correlations of clusters in the same redshift bin, but in different richness bins. Including these cross-correlations considerably enhances the signal-to-noise of our constraints on the clustering biases. Because σ_z is small for redMaPPer clusters ($\sigma_z \lesssim 0.01$) and because the redshift bins are wide ($\Delta z \sim 0.07$), the angular cross-correlations between different redshift bins are expected to be negligible and therefore contribute little information to our bias constraints. Since including these measurements would come at the cost of increasing the size of the covariance matrix — and would therefore make our jackknife covariance estimation less reliable (see below) — we do not include measurements of cross-redshift bin correlations as part of our analysis. We have, however, confirmed that these correlations are negligible. For our baseline analysis the data vector has dimension $d = N_\theta N_\lambda (N_\lambda + 1) N_z / 2 = 80$.

We compute the covariance matrix of our $w(\theta)$ measurements using a jackknife approach. To estimate the covariance matrix with a jackknife, the survey region is divided into $N_{\rm jk}$ patches. The measurement of $w(\theta)$ is repeated with each of the patches removed in turn. We use $\vec{w}_i$ to denote the estimate of $w(\theta)$ with the i-th patch removed, where the vector notation indicates that $\vec{w}_i$ includes measurements at several θ values and for several richness/redshift bins ($\vec{w}_i$ is assumed to be a column vector). The jackknife covariance matrix estimate is

$$\hat{\mathbf{C}} = \frac{N_{\rm jk} - 1}{N_{\rm jk}} \sum_i^{N_{\rm jk}} \left(\vec{w}_i - \bar{\vec{w}}\right) \left(\vec{w}_i - \bar{\vec{w}}\right)^T , \quad (7)$$

where

$$\bar{w}(\theta) = \frac{1}{N_{\rm jk}} \sum_{i=1}^{N_{\rm jk}} \vec{w}_i(\theta) \quad (8)$$

(see e.g. Norberg et al. 2009). In this work we use $N_{\rm jk} \sim 800$ patches whose edges are along lines of constant right ascension and declination. Since the data vector has 80 elements, there are roughly 10 times as many jackknife patches as the dimension of the covariance matrix.

4.1 Angular Binning

In principle, since all angular scales contain information about $w(\theta)$, one would like to measure $w(\theta)$ across the widest possible range of θ to extract the tightest possible constraints on the biases of redMaPPer clusters. At low θ, however, modeling $w(\theta)$ becomes increasingly difficult for two reasons. First, modeling the matter power spectrum at small scales is difficult because of baryonic effects (Jing et al. 2006; van Daalen et al. 2011). Second, at small scales the bias is expected to become scale-dependent, and modeling this scale dependence is difficult (see e.g. Hayashi & White 2008; Zu et al. 2012, for discussion within the context of halo-mass correlation functions).

To eliminate modeling uncertainties at small angular scales, we restrict our analysis to the angular regime for which the power spectrum can be accurately modeled and the linear bias model is expected to be valid. Imposing this requirement greatly simplifies the analysis as it leaves only one free parameter — the linear bias, b^α — to describe the clustering of redMaPPer clusters in the α richness/redshift bin (given a fixed cosmological model).

Zu et al. (2012) find that a linear bias model can adequately describe the halo-mass correlation function for scales $R \gtrsim 3.5$ Mpc. Being conservative, we therefore set $\theta_{\rm min}$ by demanding that the projected distance R spanned by the angle $\theta_{\rm min}$ be more than a minimum length $R_{\rm min} = 5\ h^{-1}$Mpc for all clusters in a given redshift bin. This amounts to setting $\theta_{\rm min} \approx 39'$ for the first redshift bin and $\theta_{\rm min} \approx 30'$ for the second redshift bin. The boundary of the lowest redshift bin has been chosen to maximize signal-to-noise while maintaining the requirement that $\theta_{\rm min} d_A(z_{\rm min}) = 5\ h^{-1}$Mpc. We emphasize that the minimum cutoff length is especially conservative in that the cutoff distance is a distance *in projection*; the true three-dimensional separation is expected to be significantly larger (≈ 25 Mpc for our cluster sample).

At large scales, modeling the $w^{\alpha\beta}(\theta)$ is straightforward, but computing the covariance of $\hat{w}^{\alpha\beta}(\theta)$ with the jackknife becomes difficult. The jackknife covariance estimate is only expected to yield reliable results for angular scales less than the size of the jackknife patches. For our $N_{\rm jk} \sim 800$ patches, the typical size of a patch is $\theta_{\rm patch} \sim 170'$. We therefore set $\theta_{\rm max} = 100'$, roughly a factor of 1.7 smaller than the size of the jackknife patches. Our four angular bins are spaced logarithmically between $\theta_{\rm min}$ and $\theta_{\rm max}$.

Fig. 1 shows the correlation matrix for the data vector as measured using the jackknife with roughly 800 subregions. The data vector is ordered such that the first 40 elements correspond to the first redshift bin and the last 40 correspond to the second redshift bin. For each redshift bin, the elements are ordered following the arrangement in Fig. A1 and Fig. A2: the first 16 elements correspond to the measurements in the first row of those figures, the next 12 elements correspond to the second row, etc. The key take away from this figure is that there is little covariance between clusters in different redshift bins, but that there is significant covariance between different richness bins within the same redshift slice.

4.2 Correction for Observational Systematics

If the density of galaxy clusters is modulated by observing conditions, the variation in observing conditions across the survey will induce artificial power in the clustering of clusters. To correct for this potential source of systematic error, we evaluate several measures of observation quality at each cluster's location — including sky flux, dust extinction, size of the point spread function and survey depth — and then bin the clusters by these measures. We then determine the area sampled by each bin, and calculate the corresponding cluster number density. In the absence of observational systematics, we expect the cluster density to be independent of the various measures of observation quality.

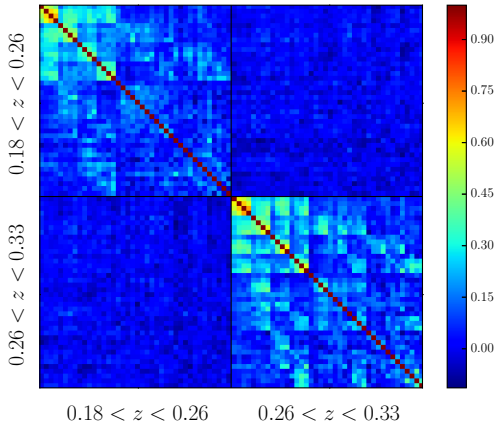

Figure 1. The full correlation matrix $\mathrm{Cov}(X_i, X_j)/\sigma_i\sigma_j$ between each measured $X_i = \hat{w}^{\alpha\beta}(\theta)$, computed using a spatial jackknife with roughly 800 subregions. See text for the ordering of the matrix elements. Note that the clustering signals from clusters in different redshift bins are uncorrelated.

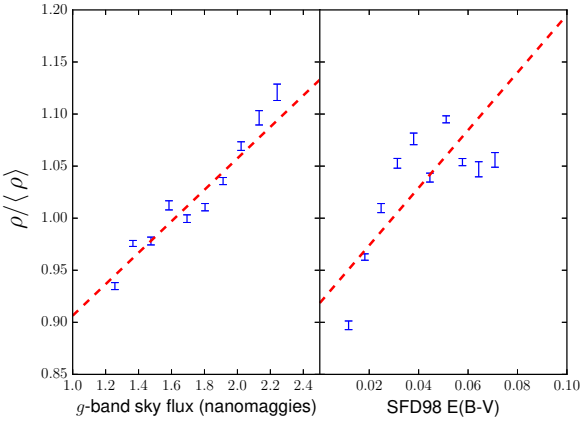

Figure 2. The measured variation in redMaPPer cluster density with g-band sky flux and $E(B-V)$ dust extinction measured by Schlegel et al. (1998). Dashed lines show the linear fits that we use to correct our clustering measurements for these variations.

Fig. 2 shows how the redMaPPer cluster density varies with both sky flux in the g-band (left panel) and $E(B-V)$ dust extinction measured by Schlegel et al. (1998) (right panel). We have selected these two potential sources of systematic contamination because they exhibit the strongest effect on the redMaPPer cluster density. Variations in g-band sky flux and dust extinction can lead to $\sim 10\%$ changes in the cluster density. In order to correct our analysis for these effects, we introduce a systematic weight, $w_i^{\rm sys}$, for the i-th cluster:

$$w_i^{\rm sys} = \frac{A + Bs_i}{\bar{n}}, \tag{9}$$

where $\bar{n}$ is the average cluster density, s_i is the measure of the observational systematic evaluated at the i-th cluster, and $A+Bs_i$ is the linear fit to the observed variations in cluster density shown as the dashed lines in Fig. 2. The weight $w_i^{\rm sys}$ is the relative over-sampling of regions that have observation quality described by s_i. Consequently, we can correct for this systematic by applying $w_i^{\rm sys}$ to each random point. We choose to only weight the random catalog by sky flux in the g-band as the correlation between this systematic and the redMaPPer cluster density appears particularly tight. In §7.5 we determine the level of systematic uncertainty introduced into our parameter constraints by this choice.

5 ANALYSIS

Given bias parameters b^α for each richness/redshift bin and a cosmological model, we can compute the predicted $w^{\alpha\beta}(\theta)$ using Eqs. 3 and 4. We compute the matter power spectrum, $P(k,z)$, in Eq. 4 using CAMB[3] (Lewis et al. 2000) with the Halofit prescription for the non-linear power spectrum (Smith et al. 2003) including the updates of Takahashi et al. (2012). At scales larger than $\sim$ 5 Mpc the influence of baryons on the matter power spectrum is expected to be at most a few percent (e.g. van Daalen et al. 2011). Since our analysis only uses scales larger than 5 h^{-1}Mpc, the effects of baryons on the matter power spectrum are well below the statistical uncertainty of our measurements. The accuracy of Halofit should therefore be sufficient for this analysis.

5.1 Bias-only Model

One way to model the bias, b^α, of each bin of clusters is to simply treat the b^α as free parameters. The results of fitting such a model to the observed cluster correlation functions are presented in §6. While constraints on the b^α are potentially useful for a cosmological analysis of redMaPPer clusters, they suffer from the drawback that the b^α depend on the richness and redshift bin choices.

An alternate and bin-independent approach is to parameterize the relationship between cluster bias and the observed richness and redshift of each cluster. This parameterization can then be constrained by fitting to the measured angular correlation function. We adopt a simple model for the richness and redshift dependence of the bias:

$$b(\lambda, z) = A_\lambda \left(\frac{\lambda}{\lambda_0}\right)^{\alpha_\lambda} \left(\frac{1+z}{1+z_0}\right)^{\beta_\lambda} \tag{10}$$

where A_λ, α_λ and β_λ are free parameters. We set $\lambda_0 = 35$ and $z_0 = 0.25$ throughout; these values are chosen because they are roughly the median richness and redshift for our sample, respectively.

When constraining the bias-richness parameterization and the mass–richness relation of redMaPPer clusters, we restrict the application of these parameterizations to clusters with $\lambda \geq 20$. As discussed in Rykoff et al. (2014), our *a priori* expectation is that the connection between galaxy clusters and individual dark matter halos is very clean at high richness, but may become more problematic with decreasing richness. The richness threshold $\lambda \geq 20$ is one we believe to be very conservative. However, the lowest richness clusters with richness $5 < \lambda < 20$ are still expected to be perfectly good mass tracers. Consequently, we model the bias of the richness bin $5 < \lambda < 20$ with a single bias parameter,

[3] `http://camb.info`

b^0 (with each redshift bin having a different b^0 parameter). Because the cross-correlations between the $5 < \lambda < 20$ clusters and the $\lambda \geq 20$ clusters contain information about the biases of the $\lambda \geq 20$ clusters, and because there are many clusters with $5 < \lambda < 20$, including these cross-correlations in our analysis significantly reduces the statistical error of our bias measurements.

For the $\lambda \geq 20$ clusters, Eq. 10 yields the bias for a cluster at a particular richness and redshift. What we measure, however, is the bias averaged over a richness/redshift bin. To model the bias of a richness/redshift bin we simply average Eq. 10 over the bin:

$$b^\alpha = \frac{1}{N_\alpha}\sum_i^{N_\alpha} b(\lambda_i, z_i), \tag{11}$$

where the sum runs over the N_α clusters in the richness/redshift bin α. Our model therefore takes into account the richness and redshift distribution of all of the clusters in the bin. Note that at this stage, our modeling is completely independent of the mass–richness relation.

5.2 Mass–observable Parameterization

Above, we parameterized the bias of the redMaPPer clusters in terms of the cluster richness and redshift. Alternatively, if both the mass–bias relationship and the mass–richness relation for redMaPPer clusters is known, one can use these relations to predict the clustering bias — and therefore the angular correlation function — of the cluster population. Parameterizing in this way allows one to use the data to constrain the mass–richness model for the redMaPPer clusters.

For clusters with $\lambda \geq 20$, we model the bias as a function of richness and redshift with

$$b(\lambda, z) = \int d\ln M\, b(\ln M, z) P(\ln M|\lambda, z), \tag{12}$$

where $P(\ln M|\lambda, z)$ describes the probability of a cluster having log-mass $\ln M$ given that it has observed richness λ and redshift z. The term $b(\ln M, z)$ is the bias of a cluster with log-mass $\ln M$ and redshift z. We adopt the best-fit model for $b(\ln M, z)$ from Tinker et al. (2010), where $b(\ln M, z)$ was calibrated using N-body simulations.

We consider a Gaussian model for $P(\ln M|\lambda, z)$:

$$P(\ln M|\lambda, z) = \frac{1}{\sqrt{2\pi\sigma^2_{\ln M}}} \exp\left[-\frac{(\ln M - \langle \ln M|\lambda, z\rangle)^2}{2\sigma^2_{\ln M}}\right]. \tag{13}$$

To parameterize $\langle M|\lambda, z\rangle$ we adopt the model

$$\langle M|\lambda, z\rangle = A(\lambda/\lambda_0)^\alpha \left(\frac{1+z}{1+z_0}\right)^\beta. \tag{14}$$

We treat $\sigma_{\ln M}$, $\ln A$, α, and β as free parameters. This parameterization is equivalent to

$$\langle \ln M|\lambda\rangle = \ln A + \alpha \ln(\lambda/\lambda_0) + \beta \ln\left(\frac{1+z}{1+z_0}\right) - \frac{1}{2}\sigma^2_{\ln M}, \tag{15}$$

which can be directly substituted into Eq. 13.[4] We set $\lambda_0 = 35.0$ and $z_0 = 0.25$ as before.

[4] We have also considered the alternate (but similar) parameterization $\langle \ln M|\lambda\rangle = \ln A + \alpha \ln(\lambda/\lambda_0) + \beta \ln\left(\frac{1+z}{1+z_0}\right)$ but find that this parameterization is more sensitive to the value of $\sigma_{\ln M}$.

5.2.1 Line of Sight Cluster Projections

Some redMaPPer objects may in fact be projections of multiple systems along the line of sight. We consider only projections of two halos since projections of three or more halos are significantly less likely and will therefore have a subdominant impact on our results. Since projections typically occur between clusters that are separated by $\Delta z \lesssim 0.02$, and the width of our redshift bins is $\Delta z \sim 0.07$, we ignore redshift differences between the two halos. In this section we suppress the z dependence of the bias for notational convenience.

We model the bias of clusters in the presence of projections via

$$b(\lambda) = (1-f) b^{\rm no-proj}(\lambda) + f b^{\rm proj}(\lambda) \tag{16}$$

where $b^{\rm no-proj}(\lambda)$ is given by Eq. 12, and $b^{\rm proj}(\lambda)$ is the bias of projected clusters of total observed richness λ. The parameter f can be thought of as the fraction of redMaPPer objects that are projected systems. To complete our model, we need to determine an expression for $b^{\rm proj}(\lambda)$.

Consider a projected cluster with richness λ that is a blend of two halos of mass M_1 and M_2. We assume that the total richness of the projected system is equal to the sum of the richnesses of the two projected halos: $\lambda = \lambda_1 + \lambda_2$, where λ_1 and λ_2 are the richnesses of the halos of mass M_1 and M_2, respectively. We define $q = \lambda_1/\lambda$, so that $q \leq 1.0$. Without loss of generality, we assume that $\lambda_1 > \lambda_2$ and so $q \geq 0.5$.

The bias of the projected pair of halos, $b^{\rm proj}(\lambda)$, should be higher than the bias of either of the individual halos since projections occur preferentially in high density regions. Consequently, $b^{\rm proj}(\lambda) \geq b(\lambda_1)$, and thus

$$b^{\rm proj}(\lambda) > \int dM_1\; b(M_1) P(M_1|q\lambda). \tag{17}$$

Furthermore, $b^{\rm proj}$ should increase as the separation between M_1 and M_2 decreases. In the limit of zero separation, one would expect the effective bias to be $b(M_1 + M_2)$, and hence $b^{\rm proj}(\lambda) \leq b(M_1 + M_2)$. Since our model has $M \propto \lambda^\alpha$, then

$$M_2 \sim M_1 \left(\frac{1-q}{q}\right)^\alpha. \tag{18}$$

We therefore obtain an upper limit to the bias of the projected system

$$b^{\rm proj}(\lambda) < \int dM_1\; b\left(M_1\left[1 + \left(\frac{1-q}{q}\right)^\alpha\right]\right) P(M_1|q\lambda). \tag{19}$$

We can smoothly interpolate between the lower limit in Eq. 17 and the upper limit in Eq. 19 by introducing a new parameter, $g \in [0, 1]$, that scales the $((1-q)/q)^\alpha$ term. Our model for the bias including projection effects is then

$$b(\lambda) = (1-f)\int dM b(M) P(M|\lambda) + f\int dM_1 b\left(M_1\left[1 + g\left(\frac{1-q}{q}\right)^\alpha\right]\right) P(M_1|q\lambda), \tag{20}$$

where $q \in [0.5, 1]$ and $g \in [0, 1]$. In the limit that $q = 1$,

there is no mass or richness in the less-rich halo and Eq. 20 recovers the un-projected expression (Eq. 12) as expected.

We adopt flat priors on q and g across their allowed ranges. Note that describing the effects of projections using a single q and a single g for all clusters is somewhat unrealistic since the values of these parameters are likely different for different projected systems. However, by keeping q and g constant across all clusters, we are effectively extremizing the effects of projections so this is a conservative approach. As for the fraction of projected clusters f, we adopt the prior $f = 0.1 \pm 0.04$ utilized in S16.

5.3 Assembly Bias

It is commonly assumed that the clustering amplitude of dark matter halos depends only on the halo mass. Assembly bias refers to the dependence of halo clustering on additional properties of the halos, such as assembly history or concentration. Assembly bias has been observed in simulations (e.g Gao et al. 2005; Wechsler et al. 2006; Jing et al. 2007) and motivated by theory (e.g. Dalal et al. 2008). Recently, Miyatake et al. (2015) (hereafter M15) have found evidence for assembly bias in a sample of SDSS redMaPPer clusters very similar to that used in this work. The results of M15 suggest that the clustering of redMaPPer clusters depends on $\overline{R}_{\rm mem}$, the mean separation of cluster member galaxies from the cluster center.

Assembly bias is a potential source of systematic error in the model we have developed above. The $b(M)$ from Tinker et al. (2010) is calibrated by averaging over all halos of fixed mass M in simulations. The redMaPPer catalog, on the other hand, is generated by selecting on richness, λ. Let γ represent some additional property of halos besides mass that affects their clustering, such as assembly history or concentration. If the distribution of γ for a richness-selected sample differs from that of a mass-selected sample, then the clustering amplitude of the redMaPPer clusters may differ from that predicted by $b(M)$, resulting in biased parameter constraints. This effect has been estimated to be negligible for SDSS clusters (Wu et al. 2008). Nevertheless, the recent detection of assembly bias by M15 suggests that this effect is significantly stronger in the data than was originally expected. Consequently, we explore the the impact of assembly bias on our mass–richness calibration results in more detail below. We also note that in addition to dependence of the halo bias on assembly history or concentration, the mass–richness relation may also be dependent on assembly history or halo concentration (Zentner et al. 2005; Mao et al. 2015).

M15 consider the dependence of cluster clustering on the mean distance between the cluster center and the cluster member galaxies, $\overline{R}_{\rm mem}$:

$$\overline{R}_{\rm mem} = \sum_i R_i P_i, \tag{21}$$

where R_i is the physical separation between the i-th member galaxy and the corresponding halo center, and P_i is the membership probability of the i-th galaxy as determined by the redMaPPer algorithm. M15 divide their cluster sample into two sets with roughly identical richness and redshift distributions, but with different $\overline{R}_{\rm mem}$ distributions. For both of these cluster samples, M15 measure the weak lensing signals around the clusters and fit these measurements with a halo model. They find that the one-halo terms for both cluster samples are consistent within errors (suggesting that the two samples have similar halo mass distributions), but that the two-halo clustering amplitudes are different. M15 also measure halo clustering directly, and find that the ratio of the clustering amplitudes for the two samples is consistent with that found in their weak lensing analysis. These results suggest that the clustering of redMaPPer clusters depends not only on the halo masses of these clusters, but also on $\overline{R}_{\rm mem}$ (see also More et al. 2016a, for further discussion).

Rather than working with $\overline{R}_{\rm mem}$ directly, it is easiest to consider $\overline{R}_{\rm mem}$ normalized by the mean value of $\overline{R}_{\rm mem}$ at a given richness and redshift. We define

$$\Delta \equiv \frac{\overline{R}_{\rm mem} - \langle \overline{R}_{\rm mem}|\lambda, z\rangle}{\langle \overline{R}_{\rm mem}|\lambda, z\rangle}, \tag{22}$$

where $\langle \overline{R}_{\rm mem}|\lambda, z\rangle$ is the mean $\overline{R}_{\rm mem}$ for clusters of richness λ and redshift z. We approximate $\langle \overline{R}_{\rm mem}|\lambda, z\rangle$ by fitting a spline to the average value of $\overline{R}_{\rm mem}$ computed across ten bins of richness and five bins of redshift.

The dependence of halo clustering on Δ can in principle affect our analysis in two ways. First, the mass–richness relationship, $P(M|\lambda)$, can depend on Δ (see e.g. Mao et al. 2015). Since the clustering amplitude depends on the halo mass, any dependence of the mass–richness relationship on Δ would induce variation in the clustering amplitude with Δ. Secondly, the relationship between halo mass and clustering, $b(M)$, could directly depend on Δ. In principle, both of these effects could be relevant to the redMaPPer clusters. However, M15 have found that their two cluster samples have nearly identical richness distributions (by construction), very different Δ distributions (also by construction), but very nearly identical lensing signals in the one-halo regime, i.e. nearly identical mean halo masses. Their results suggest (but do not require) that Δ does not severely impact the mass–richness relation, but does significantly affect the clustering amplitude. That is, we should focus on a model, $b(M, \Delta)$, in which the halo clustering amplitude is directly modulated by Δ.

We adopt a linear model for the dependence of bias on Δ:

$$b(M, z, \Delta) = b(M, z)(c_0 + c_1\Delta) \tag{23}$$

where $b(M, z)$ is the bias model from Tinker et al. (2010). Given this dependence of the bias on Δ, Eq. 12 must be replaced with

$$\begin{aligned} b(\lambda, z, \Delta) &= \int dM\ P(M|\lambda, z, \Delta) b(M, z, \Delta) \\ &= (c_0 + c_1\Delta) \int dM\ P(M|\lambda, z) b(M, z). \end{aligned} \tag{24}$$

In going from the first to the second line we have assumed that the mass–richness relationship is independent of Δ. We note that M15 found consistent values for the average mass of clusters in bins of Δ, but this does not require that there be no dependence of the mass–richness relationship on Δ. The bias for a richness/redshift bin can then be modeled as in Eq. 11, except now we include the dependence of the bias

on Δ:

$$b^{\alpha} = \frac{1}{N_{\alpha}} \sum_{i}^{N_{\alpha}} b(\lambda_i, z_i, \Delta_i). \quad (25)$$

While our model has introduced two new parameters — c_0 and c_1 — in practice these two are related. Specifically, by construction, $b(M)$ is the halo bias averaged over all halos of a given mass. Consequently, one must obtain the Tinker et al. (2010) mass–bias relation when averaging over all halos of a given mass:

$$b(M,z) \quad = \quad \langle b \rangle_{M,z} \equiv \int d\Delta\, b(M,z,\Delta) P(\Delta|M,z), \quad (26)$$

where we have defined the quantity $\langle b \rangle_{M,z}$, which represents the bias averaged over the Δ distribution, $P(\Delta|M,z)$, at fixed mass and redshift. Satisfying the above equation and substituting the ansatz of Eq. 23 yields the constraint

$$c_0 + c_1 \langle \Delta \rangle_{M,z} = 1, \quad (27)$$

where we have defined

$$\langle \Delta \rangle_{M,z} \equiv \int d\Delta\, \Delta\, P(\Delta|M,z) \quad (28)$$

as the mean Δ at fixed M and z.

Similarly, we can compute the average bias over the Δ distribution at fixed richness and redshift:

$$\begin{aligned} \langle b \rangle_{\lambda,z} &\equiv \int d\Delta\, b(\lambda,z,\Delta) P(\Delta|\lambda,z) \\ &= \int d\Delta\, (c_0 + c_1 \Delta) P(\Delta|\lambda,z) \int dM P(M|\lambda,z) b(M,z) \\ &= (c_0 + c_1 \langle \Delta \rangle_{\lambda,z}) b_0(\lambda,z) \\ &= [1 + c_1 (\langle \Delta \rangle_{\lambda,z} - \langle \Delta \rangle_{M,z})]\, b_0(\lambda,z). \end{aligned} \quad (29)$$

Here, we have defined $b_0(\lambda,z)$ via eq. 12, i.e. $b_0(\lambda,z)$ is the bias we predict in the absence of assembly bias. We have further defined

$$\langle \Delta \rangle_{\lambda,z} \equiv \int d\Delta\, \Delta\, P(\Delta|\lambda,z) \quad (30)$$

in analogy to Eq. 28.

Notice that from Eq. 29 it is clear that if the Δ distribution for a richness-selected sample of clusters is identical to the Δ distribution of halos at fixed mass, then $\langle \Delta \rangle_{\lambda,z} = \langle \Delta \rangle_{M,z}$ and the perturbation term to our prediction exactly cancels out, as it should. We can, however, simplify our expression just a bit more by noting that by definition, $\langle \Delta \rangle_{\lambda,z} = 0$. Consequently,

$$\langle b \rangle_{\lambda,z} = [1 - c_1 \langle \Delta \rangle_{M,z}]\, b_0(\lambda,z). \quad (31)$$

Thus, we see that the quantity $\langle \Delta \rangle_{M,z}$ governs the effects of assembly bias on our measurements.

To complete our model for assembly bias, we must determine the values of c_1 and $\langle \Delta \rangle_{M,z}$. In the absence of a mass-selected clusters sample, we rely instead on an SZ-selected cluster sample to estimate $\langle \Delta \rangle_{M,z}$. We use the union catalog of SZ-detected clusters from (Planck Collaboration et al. 2015c). We match the Planck cluster catalog to redMaPPer in order to calculate Δ for the Planck clusters. Note that since all Planck clusters in the redshift range of our analysis and in the SDSS footprint are identified by redMaPPer, this results in a complete sample of SZ-selected clusters (Rozo et al. 2015).

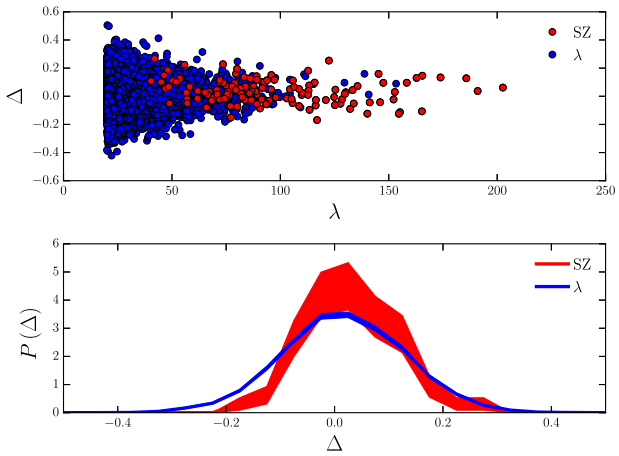

Figure 3. The top panel shows the distribution of clusters in richness (λ) and cluster member concentration (Δ) for a richness-selected sample (blue points) and an SZ-selected sample from Planck Collaboration et al. (2015c) (red points). Bottom panel shows the distribution of both of these samples as a function of Δ; the curve widths indicate the Poisson error bar on the measurement of the distribution function. Comparison of the red and blue curves in the bottom panel suggests that richness-selected clusters tend to have slightly lower values of Δ than SZ-selected clusters, meaning that richness-selected clusters are more compact on average.

The Δ distributions of the redMaPPer and Planck-selected clusters are compared in Fig. 3. The top panel of that figure shows the distribution of clusters in richness and Δ, while the bottom panel shows the distributions as a function of Δ alone. The widths of the curves in the bottom panel are the Poisson errors for each Δ bin. Making the simplifying assumption that $\langle \Delta \rangle_{M,z}$ is not strongly dependent on mass or redshift, $\langle \Delta \rangle_{M,z}$ is just the average value of Δ for all of the clusters in the SZ-matched sample. Performing this average we find $\langle \Delta \rangle_{M,z} = 0.032 \pm 0.007$. The fact that $\langle \Delta \rangle_{M,z} > 0$ (measured from the SZ-selected sample) means that SZ-selected clusters on average have larger values of $\overline{R}_{\rm mem}$ than redMaPPer clusters, i.e. redMaPPer clusters are preferentially more compact than SZ-selected clusters.

We now turn to estimating c_1, the remaining parameter in our model. Measuring c_1 with the SZ-selected sample is difficult because the small number of SZ-selected clusters means that any correlation function measurement with these clusters is very noisy. Instead, we estimate c_1 using the redMaPPer sample in the following way. In analogy to Eq. 23 we define

$$b(\lambda,z,\Delta) = \langle b \rangle_{\lambda,z} (d_0 + d_1 \Delta). \quad (32)$$

Since $\langle \Delta \rangle_{\lambda,z} = 0$ by definition, we must have $d_0 = 1$. By measuring the correlation function in bins of Δ we can fit for d_1. We then adopt the approximation $c_1 \approx d_1$.

For the purposes of estimating d_1, we divide the cluster sample into three bins of Δ and measure the angular clustering of the clusters in these bins. We then fit these measurements treating the bias in each Δ bin as a free parameter. The constraints on the bias parameters as a function of Δ

are shown as the data points with error bars in Fig. 4. The position on the x-axis of the data points is the average value of Δ for that bin. We model the bias measurements shown in Fig. 4 with

$$b_\gamma = \sum_i^{N_\gamma} b(\lambda_i, z_i)(1 + d_1\Delta_i), \quad (33)$$

where the sum runs over all N_γ clusters in the γ-th Δ bin and d_1 is treated as a free parameter. For $b(\lambda_i, z_i)$, we use the best-fit $b(\lambda, z)$ relation from the bias-only analysis described in §5.1.

The fitting procedure described above yields a constraint of $d_1 = 3.6 \pm 0.7$. We therefore find statistically significant evidence (5σ) that the clustering of redMaPPer clusters increases with Δ, in agreement with the results of M15. Using this constraint on d_1 we can compute a model prediction (using Eq. 33) for the bias of every redMaPPer cluster. These predictions, averaged over all clusters in each Δ bin are shown as the solid orange bars in Fig. 4. The extent of these bars along the x-axis indicates the width of the Δ bin, while the extent along the y-axis indicates the range allowed by the uncertainty on d_1. It is clear from the figure that our simple linear model for the dependence of the bias on Δ (Eq. 33) provides a reasonable fit to the measured biases. We have performed similar fits after dividing the redMaPPer clusters into richness bins, and find no significant evidence that d_1 varies with richness.

We now have all the ingredients necessary to compute c_0 and c_1. We approximate $c_1 \approx d_1$ and set $c_0 = 1 - c_1\langle\Delta\rangle_{M,z}$. The bias for a richness/redshift bin can then be computed using Eq. 25. In computing c_0 and c_1 we have made two significant assumptions: first, that the SZ-selected sample could be used as a reasonable proxy for a mass-selected sample when computing $\langle\Delta\rangle_{M,z}$, and second, that we could approximate $c_1 \approx d_1$. To account for the systematic error introduced by these assumptions, we take the approach of allowing $\langle\Delta\rangle_{M,z}$ and c_1 to vary in our analysis across wide, flat priors. The central values of these priors are chosen to be $\langle\Delta\rangle_{M,z} = 0.032$ and $c_1 = 3.6$, i.e. the values measured above. For the widths of the priors, we allow $\langle\Delta\rangle_{M,z}$ and c_1 to vary between 50% and 150% of their central values. These priors are summarized in Table 1.

Since we find $\langle\Delta\rangle_{M,z} > 0$, redMaPPer clusters are slightly more concentrated than SZ-selected clusters and therefore have lower value of Δ on average. Since we find $c_1 > 0$, lower values of Δ correspond to lower clustering biases. Consequently, for fixed measurements of $w^{\alpha\beta}(\theta)$, a model that includes the effects of assembly bias is expected to yield a somewhat higher normalization of the mass–richness relation. Indeed, as we show in §7.3, this is what we find.

5.3.1 *Evidence for Assembly Bias*

Given the measured dependence of the bias with Δ shown in Fig. 4, an interesting question to ask is whether or not these measurements provide evidence for assembly bias. In principle, the measured dependence of bias with Δ could be due to dependence of Δ on cluster mass. If higher mass clusters tended to have higher values of Δ, these clusters would also have higher biases because $b(M)$ is an increasing function. If this were the case, the measured dependence of the bias on Δ would not constitute evidence for assembly bias.[5]

The dependence of cluster mass on Δ must be relatively steep in order to explain the observed dependence of the bias on Δ. However, if the dependence of mass on Δ were too steep, the resultant scatter in the redMaPPer mass–richness relation would be larger than the observed scatter. The most extreme model is that *all* of the scatter in the mass–richness relation is due to the dependence of mass on Δ. If we can show that even this extreme model cannot explain the observed dependence of bias on Δ, then this constitutes evidence for assembly bias. Note that if all of the scatter in the mass–richness relation *were* due to Δ, one could calibrate a new mass–richness–Δ relationship with zero scatter.

To test the extreme model described above, we assign masses to the redMaPPer clusters using a model that does not include assembly bias, but instead maximally correlates scatter in the mass–richness relation with scatter in Δ. The i-th cluster is assigned a mass using

$$\ln M_i = \langle \ln M|\lambda_i, z_i\rangle + \frac{\Delta_i}{\sigma_\Delta(\lambda_i)}\sigma_{\ln M}(\lambda_i), \quad (34)$$

where we use our best-fit model for $\langle \ln M|\lambda_i, z_i\rangle$ and $\sigma_\Delta(\lambda)$ is the standard deviation of Δ as a function of cluster richness. We compute $\sigma_\Delta(\lambda)$ by binning clusters in richness and computing σ_Δ in each richness bin; $\sigma_\Delta(\lambda)$ is computed at arbitrary richness by linear interpolation. We assume that the scatter in the mass–richness relation is described by

$$\sigma^2_{\ln M}(\lambda) = \alpha^2\left[\sigma^2_{\ln\lambda|M} + (1/\lambda).\right] \quad (35)$$

The form of this scatter reflects the population statistics of dark matter substructures in host halos as found in numerical simulations (e.g. Boylan-Kolchin et al. 2010; Mao et al. 2015). We assume the intrinsic scatter in mass at fixed richness for high mass clusters (where the $1/\lambda$ term becomes negligible) is $\sigma_{\ln M|\lambda} = \alpha\sigma_{\ln\lambda|M} = 0.3$. This is a conservative choice; Rozo & Rykoff (2014) and Rozo et al. (2015) constrain $\sigma_{\ln M|\lambda} \approx 0.25$, including the Poisson contribution. By setting $\sigma_{\ln M|\lambda} = 0.3$, we are over-estimating the impact that mass-scatter can have on the clustering bias prediction.

The mass assignments described by Eq. 34 effectively attributes all of the scatter in the mass–richness relation to variation in Δ. With the masses assigned to each cluster using the no-assembly-bias model of Eq. 34, we compute the average bias of each Δ bin in Fig. 4 using the $b(M)$ relation from Tinker et al. (2010). These average biases and the corresponding error bars are shown as the green solid regions in Fig. 4. It is clear from the figure that the no-assembly-bias model is a worse fit to the bias measurements than our fiducial assembly bias model (i.e. Eq. 23). We find $\chi^2 = 5.4$ for the no-assembly-bias model, with a probability to exceed of 6.7% (one degree of freedom is used to fit for the mean bias).

[5] The measurements of M15 suggest that Δ does *not* depend strongly on cluster mass since the one-halo contributions to the weak lensing signals of these two samples are nearly identical. Our goal here, however, is to determine whether or not our clustering measurements support the assembly bias picture in the absence of the mass measurements by M15.

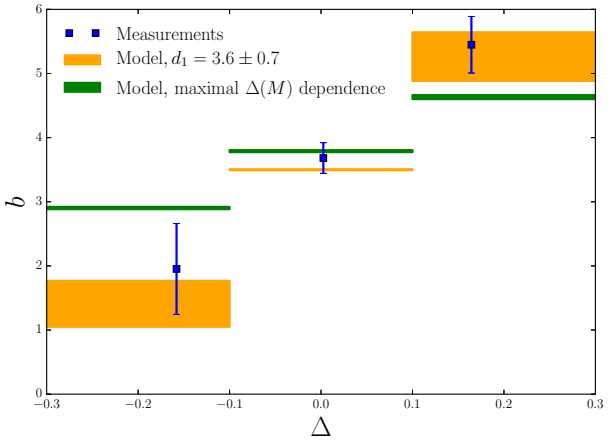

Figure 4. Clustering bias (b) as a function of cluster member concentration (Δ) for three Δ bins (blue points). The cluster sample used in this plot has been restricted to $\lambda \geq 20$. Orange regions show the best-fit assembly bias model prediction (Eq. 23) for the mean bias of each Δ bin. The vertical extent of the regions indicates the range allowed by the uncertainty on the model parameter d_1. The green regions represent the biases predicted by a model that does not include assembly bias, but instead assumes that cluster mass and Δ are maximally correlated (Eq. 34). The vertical extent of the green regions represents the error on the mean bias in this model. The model that includes assembly bias is a better fit to the clustering bias measurements than the model that does not include assembly bias.

The measured bias values can therefore be taken as weak evidence for assembly bias. This statement is quite conservative since we have assumed a large value ($\sigma_{\ln M} = 0.3$) for scatter in the $\ln M$–richness relation in Eq. 35, and since we have assumed that Δ and cluster mass are maximally correlated. If the $\sigma_{\ln M}$ were reduced, or if Δ and mass are not maximally correlated, the tension between the no-assembly-bias model and the measured biases would increase. Note that if Δ and halo mass *were* maximally correlated, one could construct a zero-scatter mass-proxy as some combination of λ and Δ; the implausibility of this scenario suggests that Δ and halo mass are almost certainly not maximally correlated.

5.3.2 Calibration Uncertainty in $b(M)$

Tinker et al. (2010) find scatter around the $b(M)$ measured across different simulations of roughly 6%. Such scatter contributes a fundamental source of uncertainty to the mass–richness constraints we derive using $b(M)$. We introduce this uncertainty into our model by multiplying $b(M)$ by $(1 + b_{\rm scaling})$, where $b_{\rm scaling}$ is a new parameter of our model. We place a Gaussian prior on $b_{\rm scaling}$ centered at zero with $\sigma = 0.06$. In principle, simply scaling $b(M)$ by $(1 + b_{\rm scaling})$ may not fully capture the cross-simulation variation observed by Tinker et al. (2010). However, this is a reasonable approach given that we do not have probability distributions for all of the parameters of the Tinker et al. (2010) bias model. Correctly modeling the uncertainty in $b(M)$ will be an important part of future attempts to use cluster clustering to constrain mass–observable relations.

5.4 Likelihood Analysis

We adopt a Gaussian likelihood for the data given the model:

$$\mathcal{L}(\vec{d}|\vec{p}) \propto \exp\left[-\frac{1}{2}\left(\vec{d}-\vec{m}(\vec{p})\right)^T \mathbf{C}^{-1}\left(\vec{d}-\vec{m}(\vec{p})\right)\right], \quad (36)$$

where $\vec{d}$ is the data vector (containing all the cross-richness correlation function measurements) and $\vec{m}(\vec{p})$ is the model vector, which is a function of the parameter vector, $\vec{p}$. We compute $\mathbf{C}^{-1}$ using the estimator from Hartlap et al. (2007):

$$\widehat{\mathbf{C}^{-1}} = \frac{N-d-2}{N-1}\mathbf{C}^{-1}, \quad (37)$$

where N is the number of jackknife regions (in this case $N = 800$), d is the length of our data vector (in this case $d = 80$) and $\mathbf{C}$ is the covariance matrix estimated from the jackknifing procedure.

We remind the reader that we perform two fits to the data: one in which the bias values themselves are the free parameters, and the other using a parameterized version of the mass–richness relationship and the $b(M)$ relation from Tinker et al. (2010). For reference, we reproduce here the complete model for the bias of the α-th richness/redshift bin:

$$b^\alpha = \frac{1}{N_\alpha}\sum_i^{N_\alpha}(c_0 + c_1\Delta_i)b_{\rm scaling} \times \left[(1-f)\int dM b(M,z_i)P(M|\lambda_i,z_i) + f\int dM_1 b\left(M_1\left[1+g\left(\frac{1-q}{q}\right)^\alpha\right]\right)P(M_1|q\lambda_i,z_i)\right], \quad (38)$$

where $P(M|\lambda_i, z_i)$ is given by Eq. 13. As stated above, we do not model the biases of the low-richness clusters ($5 < \lambda < 20$) with Eq. 38, but instead treat the biases of each low richness bin (one for each redshift bin) as a free parameter.

The analysis of Rozo & Rykoff (2014) and Rozo et al. (2015) suggests that the scatter in the mass–richness relationship is $\sigma_{\ln M} \sim 0.2 - 0.3$. In this analysis, we treat $\sigma_{\ln M}$ as a free parameter, imposing a flat prior $\sigma_{\ln M} \in [0.05, 0.5]$. We find little degeneracy between $\sigma_{\ln M}$ and A or α. We marginalize over $\sigma_{\ln M}$ in the constraints presented below. The priors on all of our model parameters are summarized in Table 1. These priors, combined with the likelihood in Eq. 36 allow us to compute the posterior on the parameters of our model given the observed data. We use a Markov Chain Monte Carlo approach to sample this multi-dimensional posterior. We perform the sampling using `emcee` (Foreman-Mackey et al. 2013). The entire analysis pipeline (from calculating $w_M(\theta)$ to sampling the posterior) is implemented in the `CosmoSIS`[6] framework (Zuntz et al. 2015).

5.5 Simulations

In order to validate our approach to measuring the mass–richness relationship of redMaPPer clusters, we apply the

[6] `https://bitbucket.org/joezuntz/cosmosis/wiki/Home`

Table 1. Priors and posteriors on parameters of mass–richness parameterization. The parameters $\ln A$, α, β and σ govern the amplitude, slope in richness, slope in mass, and scatter of the mass–richness relationship of redMaPPer clusters, respectively. The parameter f is the fraction of clusters that are projections, q is the fraction of mass in the dominant halo of a projection, and g governs the magnitude of projection effects. The parameter $b_{\rm scaling}$ controls the uncertainty in the model $b(M)$ from Tinker et al. (2010). The parameters $\langle\Delta\rangle_{M,z}$ and c_1 govern the assembly bias of redMaPPer clusters. The parameters f, q, g, $b_{\rm scaling}$, $\langle\Delta\rangle_{M,z}$, c_1, and σ are all nuisance parameters that we marginalize over. Priors of the form $[A, B]$ are flat with minimum and maximum given by A and B; priors of the form $A \pm B$ are Gaussian with mean given by A and standard deviation given by B. Posteriors are represented in terms of the mean and standard deviation.

Parameter	Description	Prior	Posterior
b^{0,z_0}	Bias of $5 < \lambda < 20$, $0.18 < z < 0.26$ clusters	$[0.2, 10.0]$	1.85 ± 0.05
b^{0,z_1}	Bias of $5 < \lambda < 20$, $0.26 < z < 0.33$ clusters	$[0.2, 10.0]$	1.74 ± 0.05
$\ln(A/M_\odot)$	Amplitude of mass–richness relation	$[30.0, 35.0]$	33.66 ± 0.18
α	Richness scaling of mass–richness relation	$[-0.5, 4.0]$	1.18 ± 0.16
β	Redshift scaling of mass–richness relation	$[-20.0, 20.0]$	1.86 ± 2.4
σ	Scatter in mass–richness relation	$[0.05, 0.5]$	—
f	Projection fraction	0.10 ± 0.04	—
q	Projection effects	$[0.5, 1.0]$	—
g	Projection effects	$[0.0, 1.0]$	—
$b_{\rm scaling}$	Uncertainty in $b(M)$	0.00 ± 0.06	—
$\langle\Delta\rangle_{M,z}$	Assembly bias	$[0.011, 0.053]$	—
c_1	Assembly bias	$[0.95, 3.95]$	—

analysis pipeline that we have developed to a mock data set generated from simulations. We use an N-body simulation of a flat-ΛCDM cosmological model with $\Omega_M = 0.286$, $h_0 = 0.7$, $\Omega_b = 0.047$, $n_S = 0.96$, and $A_s = 2.1 \times 10^{-9}$, run with 1400^3 particles in a box 1050 Mpc h^{-1} on a side, with the L-Gadget code, a variant of Gadget (Springel 2005). A lightcone was output from the simulation on the fly, to produce a quarter-sky simulation over the same redshift range as the data. We use a halo catalog generated by the Rockstar halo finder (Behroozi et al. 2013), run directly on the dark matter lightcone.

The probability that a halo of mass M has richness λ, $P(\lambda|M)$, can be related to our parameterized $P(M|\lambda)$ using Bayes' theorem: $P(\lambda|M) \propto P(M|\lambda)P(\lambda)$. The mass–richness relation $P(M|\lambda)$ is given by Eqs. 13 and 14. We determine the prior $P(\lambda)$ from the real data by fitting a Schechter function to the observed distribution of λ. We randomly draw from $P(\lambda|M)$ to generate a simulated value of λ for each mock halo.

We choose the parameters A, α and β of the mass–richness relation to ensure that the distribution of simulated clusters in richness and redshift is close to the distribution of real clusters. Since the cosmological model used to generate the simulation used herein is slightly different from the currently favored ΛCDM cosmological model, it stands to reason that matching the observed cluster abundance will require somewhat different mass–richness parameters than are obtained from our analysis of the data. We find that setting $\ln(A/M_\odot) = 33.15$, $\alpha = 1.0$, $\beta = 1.0$, and $\sigma_{\ln M} = 0.2$ results in a cluster catalog that has roughly the same number density of clusters as the SDSS data.

The simulated redMaPPer catalog does not include the effects of line-of-sight projections of clusters, because we use a pure halo catalog generated using the three-dimensional positions of the dark matter particles. As a result, two halos that happen to be close together on the sky will never be lumped into the same simulated redMaPPer object. For this reason, when analyzing the simulation data we fix $f = 0$. Furthermore, while the simulations include the effects of assembly bias in the halos, without a more comprehensive modeling approach, we do not know an appropriate value of Δ to assign to each cluster. We therefore fix $\langle\Delta\rangle_{M,z} = 0$ and $c_1 = 0$ when analyzing the simulated redMaPPer catalog.

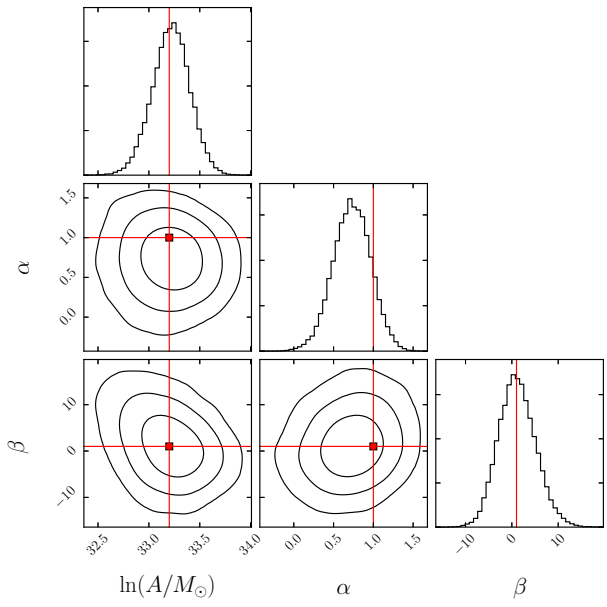

Figure 5. Posteriors on the parameters of the mass–richness relation resulting from the analysis of a simulated cluster catalog generated from N-body simulations. Contour lines enclose 68%, 95% and 99.7% of the probability density. Input values are shown by the red lines. Our analysis successfully recovers the input parameters of the mass–richness relation.

We apply the same analysis pipeline to the simulated data as to the real data. This includes the process of pair counting, jackknifing to determine the covariance matrix, and fitting for the mass–richness parameters. When computing $w_M(\theta)$ for the analysis of the simulated data we use the same cosmological model that was used to generate the N-body simulations.

Table 2. Marginalized constraints on the biases of redMaPPer clusters in bins of richness and redshift.

Richness range	$0.1 < z < 0.26$	$0.26 < z < 0.33$
$5 < \lambda < 20$	$b = 1.85 \pm 0.06$	$b = 1.74 \pm 0.05$
$20 < \lambda < 28$	$b = 2.8 \pm 0.2$	$b = 3.0 \pm 0.2$
$28 < \lambda < 41$	$b = 3.1 \pm 0.3$	$b = 3.7 \pm 0.3$
$41 < \lambda < \infty$	$b = 4.6 \pm 0.3$	$b = 5.1 \pm 0.4$

Fig. 5 shows the constraints obtained on the mass–richness parameters by applying our pipeline to the simulated data. The input mass–richness parameters are shown as the red lines, and contour lines represent 1σ, 2σ, etc. As evidenced by the figure, our analysis appears to correctly extract the input model parameters. We find $\chi^2/\text{d.o.f.} = 70.7/73$, suggesting that the model is an excellent fit to the data. Furthermore, we find that the error bars on the extracted model parameters are similar to those found in our analysis of the real data.

6 RESULTS

Figures showing the measured angular correlation functions and the best fit models are collected in Appendix A, Figs. A1 and A2. The best-fitting models for the bias-only parameterization are shown in red, while the best-fitting mass–richness models are shown in green. The results of these two fits are very similar (in many cases the two curves are indistinguishable by eye). This suggests that the mass–richness parameterization is well matched to the true clustering biases of the redMaPPer clusters.

We find somewhat low values of χ^2, with $\chi^2/\text{d.o.f.} = 57.1/72$ for the bias-only model, and $\chi^2/\text{d.o.f.} = 57.5/75$ for the mass–richness model.[7] The probabilities for χ^2 to be less than the quoted values are roughly 10% and 6%, respectively. We caution, however, that since the covariance matrix is estimated using a Jackknife approach, there are noise fluctuations in the covariance matrix that can increase or reduce the recovered scatter. Roughly speaking, if our error bars on the correlation function measurements were reduced by $\sim 10\%$, we would have $\chi^2/\text{d.o.f.} \sim 1$. As we show below, our error bars on the parameters of the mass–richness relation are dominated by uncertainty in the model parameters. A 10% reduction in the measurement errors would therefore have little impact on our results.

Table 2 summarizes the constraints on the clustering biases for each individual richness/redshift bin. As expected, the bias increases steadily with increasing richness.

Fig. 6 shows the constraints on the parameters of the mass–richness relation derived from the angular clustering measurements.[8] The value of $\ln A$ — the amplitude parameter of the mass–richness relationship — is constrained to be $\ln(A/M_\odot) = 33.66 \pm 0.18$, corresponding to an 18% mass constraint. The slope of the mass–richness relationship is constrained to be $\alpha = 1.18 \pm 0.16$. The scaling with redshift

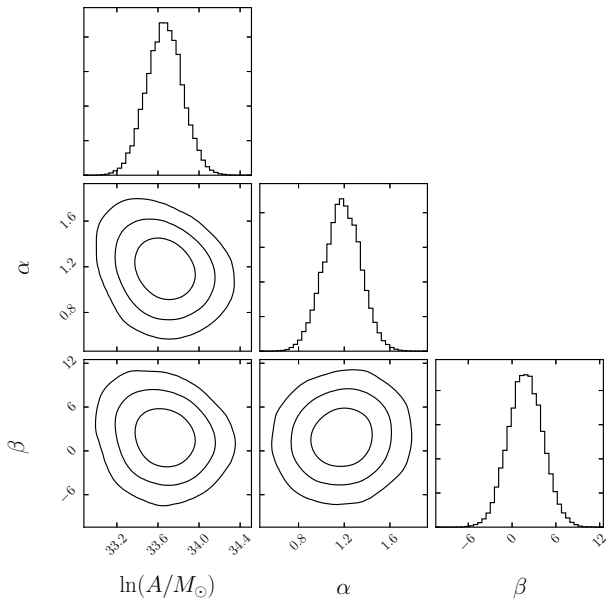

Figure 6. Constraints on the parameters of the mass–richness relationship obtained from a fit to the measured angular correlation functions. Contour lines enclose 68%, 95% and 99.7% of the probability density.

is constrained to be $\beta = 1.86 \pm 2.4$; the weakness of this constraint is due in part to our use of only two redshift bins and the fact that our cluster sample is narrowly distributed in redshift. These constraints are summarized in the 'Posterior' column of Table 1.

Our calibration can be compared to the weak lensing mass estimator of S16. We emphasize that despite common authors between this work and S16, no comparison between the two analyses was performed before the analyses pipelines were finalized. Our decision to focus on the NGC exclusively did come after a comparison with S16 had occurred, though we believe we are well justified in our choice.

S16 provides the current best weak lensing mass calibration of redMaPPer clusters, and they discuss in detail how their mass calibration compares to others in the literature. While the constraints on the slope of the mass–richness relation are in good agreement between the two works, there is mild tension on the recovered amplitude assuming our fiducial cosmology, with the clustering-derived constraints preferring a somewhat higher amplitude. At the richness pivot point used in this work, $\lambda_0 = 35$, S16 predicts $\log_{10}(M/M_\odot) = 14.43 \pm 0.04$, while our constraints yield $\log_{10}(M/M_\odot) = 14.62 \pm 0.08$; this discrepancy corresponds to roughly 2.2σ tension. Because the clustering analysis prefers a slightly lower value of α than the weak lensing analysis, this tension is reduced for $\lambda > 35$. For $\lambda < 35$, the tension remains roughly the same since the error bars increase as one moves away from the λ pivot point. We postpone a discussion of the origin of this tension, and a more detailed comparison of the two results, to future work. That is, our current results reflect our best understanding of both the weak lensing and clustering analysis prior to the comparison of the two works.

We have also considered a power-law bias-richness re-

[7] When calculating the d.o.f. for the mass–richness model, we do not include the various systematic parameters that have small impacts on our model predictions.

[8] Contour plots were made using `corner.py` (Foreman-Mackey et al. 2016).

lation as per Eq. 10. This model has five parameters: A_λ, α_λ, β_λ and two bias parameters for $5 < \lambda < 20$ clusters in the two redshift bins. Fitting this model to the data, we find $A_\lambda = 3.54 \pm 0.13$, $\alpha_\lambda = 0.57 \pm 0.08$ and $\beta_\lambda = 2.0 \pm 1.1$ with $\chi^2/\mathrm{d.o.f.} = 57.7/75$.

7 CHARACTERIZING THE UNCERTAINTY IN THE MASS–RICHNESS RELATION

The uncertainties on the mass–richness parameters presented in Fig. 6 and Table 1 receive contributions from several sources: statistical noise in the measurement of the angular correlation functions, uncertainty on the parameters of the line-of-sight projection model, uncertainty on the parameters of the assembly bias model, and scatter around the $b(M)$ relation from Tinker et al. (2010). In addition to these sources of scatter that are explicitly included in our model, it is also possible that our measurement is affected by systematic biases that we have not modeled. Below, we determine the approximate contributions of both modeled sources of scatter and unmodeled systematic errors to the uncertainty budget of our parameter constraints.

7.1 Statistical Noise in the Correlation Function Measurement

We first investigate how statistical noise in the measurement of $w^{\alpha\beta}(\theta)$ contributes to our parameter uncertainties. The contribution of statistical noise to our parameter uncertainties can be determined by setting the parameters of the line-of-sight projection model, the parameters of the assembly bias model, and b_{scaling} to constant values rather than allowing these parameters to vary. Any uncertainty in our parameter constraints that remains after fixing these model parameters must be due to measurement noise alone.

For the purposes of this test, we fix $f = 0.1$, $q = 0.75$, $g = 0.5$, $\langle\Delta\rangle_{M,z} = 0.032$, $c_1 = 3.6$ and $b_{\mathrm{scaling}} = 0$, corresponding to the central values of the priors on these parameters. The results of this section are relatively insensitive to the precise values that we choose here. Upon re-fitting this constrained model to the data, we find that the posterior on $\ln A$ is significantly tighter than that obtained in our fiducial analysis. In other words, the uncertainty on the amplitude of the mass–richness relation is dominated by uncertainty on the model parameters that we marginalize over. In the absence of uncertainty on these model parameters, the error on $\ln A$ would be only ~ 0.07 instead of ~ 0.18. Statistical noise in the measurement of $w^{\alpha\beta}(\theta)$ contributes only $\sim 10\%$ of the variance of our baseline constraint on $\ln A$.

On the other hand, we find that statistical measurement error contributes $\sim 70\%$ of the variance of our constraints on α and β. The uncertainties on these parameters would be significantly reduced with a larger cluster catalog distributed over a wider redshift range.

7.2 Scatter around $b(M)$ from Tinker et al. (2010)

Our fiducial analysis assumes a scatter of 6% around the the $b(M)$ model from Tinker et al. (2010), parameterized with b_{scaling}. To measure the contribution of this source of scatter to our parameter uncertainties, we consider a model that allows b_{scaling} to vary with the fiducial prior, but that fixes all other model parameters to the values given in §7.1. Comparing the posteriors obtained from fitting this model to the data to those obtained in §7.1 provides a measure of the contribution of uncertainty on b_{scaling} to our final parameter uncertainties.

We find that uncertainty on b_{scaling} dominates the uncertainty on $\ln A$, contributing roughly 60% of the variance of our fiducial constraint on this parameter. In other words, our constraint on the normalization of the mass–richness relation for redMaPPer clusters is currently limited by uncertainty in the $b(M)$ relation. In contrast, the posteriors on α and β are less affected by uncertainty on b_{scaling}; uncertainty on b_{scaling} contributes only $\sim 30\%$ of the variance of our constraints on these parameters.

7.3 Uncertainty on Assembly Bias Parameters

To evaluate the contribution of uncertainty on the assembly bias parameters c_1 and $\langle\Delta\rangle_{M,z}$ to our constraints on the mass–richness parameters, we fit a model to the data that allows the assembly bias parameters to vary over their fiducial priors, but that keeps the other model parameters fixed to the values in §7.1. We find that uncertainty on the assembly bias parameters contributes roughly 30% of the variance of our baseline constraint on $\ln A$, but contributes negligibly to the variance of the constraints on α and β. Uncertainty on the assembly bias parameters therefore contributes a level of uncertainty on the normalization of the mass–richness relation that is greater than that of measurement uncertainty.

We also evaluate how much the inclusion of assembly bias effects shifts our parameter constraints relative to a model that does not include these effects. We fit the data with a model that has $\langle\Delta\rangle_{M,z} = 0.0$ and $c_1 = 0$, but otherwise is identical to the baseline analysis. The results of this fit suggest that the inclusion of assembly bias in our analysis causes our best-fit $\ln A$ to increase by roughly 15%, corresponding to 0.8σ. The direction of this shift is as anticipated in §5.3. The inclusion of assembly bias effects has a smaller impact on the best-fit values of α and β.

7.4 Uncertainty on Line-of-sight Projection Parameters

We follow a similar approach to that outlined in §7.3 to estimate the contribution of uncertainty on the line-of-sight projection parameters f, q and g to our mass–richness parameter uncertainties. We fit a model to the data that allows the projection parameters to vary over the priors in Table 1, but which has the assembly bias and b_{scaling} parameters fixed to the same values as in §7.1. Comparing the parameter uncertainties obtained using this constrained model to the parameter uncertainties obtained in §7.1 suggests that uncertainty on the projection parameters contributes less than 10% of the variance of $\ln A$, α, and β.

We can also ask how much line-of-sight projections shift our parameter constraints relative to an analysis that does not account for projections. To do this, we fit a model to the data that has $f = 0.0$, but otherwise is identical to the baseline model. Analyzing the data with this model reveals that including line-of-sight projections in our analysis shifts

the maximum likelihood values of $\ln A$, α, and β by less than 0.1σ.

7.5 Systematics in $w^{\alpha\beta}(\theta)$ Measurement

As described in §4.2, we apply weights to the redMaPPer random catalog to correct for an observed dependence of the cluster density on the g-band sky flux. A similar variation in the cluster density is also observed with the $E(B-V)$ dust extinction maps from Schlegel et al. (1998) (see Fig. 2). To determine the level of systematic error introduced into our measurements by only correcting for the correlation between cluster density and g-band sky flux, we repeat the correlation function measurement and fitting using a random catalog weighted instead by $E(B-V)$ dust extinction.

We find that the application of the $E(B-V)$ weights causes our best-fit $\ln A$, α, and β to change by less than 0.05σ. This suggests that the systematic error introduced by only correcting for variations in cluster density with i-band PSF is small compared to our error bars.

As mentioned above, the results presented thus far were derived using only the NGC region of SDSS. We have also applied our clustering analysis to the SGC region. We find some tension between the clustering measurements in both regions, with the SGC preferring somewhat higher values of $\ln A$ and somewhat lower values of α than the NGC. Considering the bias-only parameterization, we find the amplitude of the bias–mass relation to be consistent between the two regions. However, the constraints on α_λ for the two regions differ by 2.1σ. There is also roughly 2.4σ tension in the biases of the clusters in the richness/redshift bin $5 < \lambda < 20$, $0.18 < z < 0.26$ between the two regions. There is no significant tension in the β_λ constraints between the two regions. When considering constraints on the mass–richness parameterization, the tension between NGC and SGC is reduced because the marginalization over $b_{\rm scaling}$ and the assembly bias parameters effectively increases the error bars on the parameters. Tension in the $\ln A$ constraints from the two regions is only 0.3σ, while tension on α is 2σ.

If the clustering of redMaPPer clusters is different in the NGC and the SGC, one might expect the abundance of redMaPPer clusters to also be different in the NGC and the SGC. Fig. 7 shows a comparison of the cluster density as a function of richness between the NGC and the SGC. The error bars in the figure only include the Poisson contribution and not sample variance. In general, the agreement between the two regions with respect to cluster abundance appears to be quite good. However, we find $\chi^2/\text{d.o.f.} = 43.7/26$ for the low redshift bin. The high value of χ^2 is driven almost entirely by clusters with $\lambda \sim 10$. For the high redshift bin, we find $\chi^2/\text{d.o.f.} = 34.8/26$. Note, though, that by only including the Poisson contribution to the error bars, we have over estimated the tension between the NGC and SGC in this comparison.

In summary, we find some evidence for tension between the clustering-derived parameter constraints in the NGC and SGC. This tension is most pronounced for our constraints on α: the NGC prefers a higher value of α than the SGC by roughly 2σ. Tension between the two regions with respect to the other mass–richness parameters is consistent with noise. There is also some evidence for tension in the abundance of low redshift, $\lambda \sim 10$ clusters between the two regions. We note that Tojeiro et al. (2014) also found evidence for tension between the NGC and SGC at low redshift ($z < 0.25$) in their measurements of the clustering of galaxies identified in SDSS. Since the origin of this tension is not well understood at this time, we refrain from combining the parameter constraints obtained from the NGC and SGC, and instead present only the results for the NGC. This choice also has the advantage that it makes comparison to the weak lensing mass constraints from S16 more straightforward since the S16 analysis was only applied to clusters in the NGC.

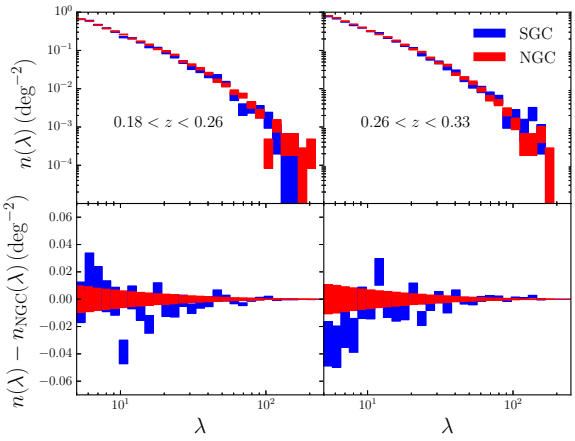

Figure 7. Cluster density as a function of richness for the NGC and SGC regions. We find some evidence for tension in the abundance of clusters between the NGC and SGC; this tension is driven by low-redshift clusters with $\lambda \sim 10$.

7.6 Jackknife Covariance Estimation

Our jackknife estimate of the covariance matrix does not show any obvious evidence for systematic errors. However, we feel it necessary to confirm that our covariance estimate is robust with respect to the choice of jackknife regions. To do this, we repeat the jackknifing procedure with 10% fewer jackknife regions (720 instead of ~ 800). Re-fitting the correlation function measurements for the mass–richness parameters using the modified covariance estimate leads to small shift in the best-fit mass–richness parameters, all well within the error bars. The largest shift observed is in the best-fit value of α, which changes by 0.23σ. Given the smallness of these shifts compared to the error bars, any uncertainty in our mass–richness constraints introduced by the choice of jackknife regions can be safely ignored.

8 COSMOLOGY DEPENDENCE

The results presented above have assumed a fixed cosmological model. In this section, we vary the cosmological parameters and re-fit the data to determine how the mass–richness relation varies with cosmology. We focus here on Ω_M, A_S and h_0. Other cosmological parameters are expected to have a subdominant effect on the predicted correlation function.

We compute the maximum likelihood mass–richness parameters at 12 points in (Ω_M, A_S, h) parameter space. These

points are chosen to be within 10% of the fiducial values of Ω_M, A_S and h_0 since Planck Collaboration et al. (2015b) constrains these parameters to better than 10%. Furthermore, restricting Ω_M, A_S and h_0 to a narrow interval ensures that the dependence of the mass–richness relation on these parameters is close to linear over the sampled range. For each point (Ω_M, A_S, h) we determine the maximum likelihood values of $\ln A$, α, and β given our correlation function measurements. Using linear regression, we then compute the dependence of $\ln A$, α, and β on Ω_M, A_S and h_0.

For the amplitude parameter, $\ln A$, we find a best fit linear model:

$$\ln(A/M_\odot) = 33.68 + 2.9\delta\Omega_M + 1.0\delta A_s + 1.8\delta h \quad (39)$$

where we have defined

$$\delta\Omega_M = \frac{\Omega_M - 0.3089}{0.3089} \quad (40)$$

$$\delta A_S = \frac{A_S - 2.141\times10^{-9}}{2.141\times10^{-9}} \quad (41)$$

$$\delta h = \frac{h - 0.6774}{0.6774} \quad (42)$$

as the fractional departures of Ω_M and A_S from the values assumed in our baseline analysis. We find that 10% changes in Ω_M, A_S and h_0 result in 1.6σ, 0.6σ and 1.0σ shifts in $\ln A$, respectively. Note that Ω_M, A_S and h_0 are constrained to $\sim 2\%$ by Planck Collaboration et al. (2015b); the variation in $\ln A$ as a function of Ω_M, A_s and h_0 over the range allowed by Planck is therefore below the uncertainty on $\ln A$.

We find that α is most senstive to Ω_M and h_0, with no significantly measured dependence on A_S over the range of A_S values considered. Our best fit relation is

$$\alpha = 1.17 - 0.6\delta\Omega_M - 0.5\delta h. \quad (43)$$

Changing Ω_M and h_0 by 10% therefore changes α by 0.4σ and 0.3σ, respectively. Any dependence of α on A_S is significantly below our error bar on α.

We find the β is most sensitive to h_0, with a best-fit linear relationship described by

$$\beta = 1.8 + 1.1\delta_h. \quad (44)$$

A 10% change in h_0 therefore results in a 0.05σ change to β. The dependence of β on Ω_M and A_S is well below our error bar on β and we do not report it here.

9 DISCUSSION

We have measured the angular correlation function of redMaPPer clusters identified in SDSS data. By fitting models to these measurements, we have extracted constraints on several parameters describing the clustering biases and mass–richness relationship of redMaPPer clusters. Our constraints on the biases of redMaPPer clusters in bins of richness and redshift are shown in Table 2. Our constraints on the mass–richness relationship for redMaPPer clusters are shown in Fig. 6 and summarized in Table 1.

We measured the correlation between clustering bias and Δ, where Δ is related to the concentration of member galaxies and is defined in Eq. 22. These measurements support the results of M15 and More et al. (2016b). Expanding on those works, we have also measured the slope of the bias-Δ relationship. Furthermore, our clustering measurements provide evidence for assembly bias independent of the weak lensing measurements of M15. Even if one assumes that Δ and mass are maximally correlated, the clustering measurements shown in Fig. 4 cannot be explained without invoking assembly bias. Finally, we find that the inclusion of assembly bias effects in our analysis increases the best-fit amplitude of the mass–richness relationship by $\sim 15\%$, reflecting the fact that the signal seen by M15 is significantly larger than was expected *a priori*.

In the absence of systematic sources of uncertainty, our analysis constrains the amplitude of the mass–richness relation to $\sim 7\%$. Including systematic sources of uncertainty, however, degrades our constraint on the amplitude of the mass–richness relation to 18%. The dominant source of systematic uncertainty is scatter around the $b(M)$ relation from Tinker et al. (2010), which makes up roughly 60% of the variance in our final constraint on $\ln A$. Uncertainty on the assembly bias parameters is the next largest source of systematic error affecting our constraint on $\ln A$, and contributes a level of uncertainty on this parameter that is greater than the uncertainty due to measurement noise. We find that line-of-sight projection effects have a negligible impact on our parameter constraints. On the other hand, our constraints on the slope parameters of the mass–richness relation — α and β — are not as strongly affected by systematic uncertainties and are currently statistics limited.

We emphasize that future measurements of cluster clustering with e.g. the Dark Energy Survey can significantly reduce the statistical uncertainty on the measured correlation functions, and enable the assembly bias parameters to be measured more tightly. In particular, we note that the larger the volume probed, the lower the errors, so cluster-clustering is particularly well suited for calibrating the mass–richness relation of high redshift clusters, exactly where the statistical and systematic uncertainty in weak lensing mass calibration is greatest. Critically, the current errors in the recovered mass–richness relation are systematic dominated, with the dominant systematic being theoretical uncertainty in the calibration of the bias–mass relation of dark matter halos. Thus, unlike weak lensing mass calibration efforts, a path towards improved mass calibration from cluster clustering is very straight forward: one just needs to implement a simulation program geared toward improving the calibration of halo bias. The prospect of improved data sets, reduced statistical errors, and a straight forward path towards reducing systematic uncertainties all bode well for the future of cluster-clustering as a method for calibrating the mass–richness relation of galaxy clusters.

ACKNOWLDEGEMENTS

This work received partial support from the U.S. Department of Energy under contract number DE-AC02-76SF00515 and from the National Science Foundation under NSF-AST-1211838. EB and BJ are partially supported by the US Department of Energy grant DE-SC0007901. We thank Matthew Becker and Michael Busha for their contributions to the N-body simulations used in this work, and Yao-Yuan Mao for helpful discussions about assembly bias. We thank Mike Jarvis for developing `treecorr` and for help with running it. We thank Melanie Simet, Rachel Mandel-

baum, and Gary Bernstein for useful discussions related to this work.

REFERENCES

Aihara H., et al., 2011, ApJS, 193, 29
Albrecht A., et al., 2006, ArXiv Astrophysics e-prints,
Baxter E. J., Rozo E., 2013, ApJ, 779, 62
Behroozi P. S., Wechsler R. H., Wu H.-Y., 2013, ApJ, 762, 109
Benson B. A., et al., 2013, ApJ, 763, 147
Boylan-Kolchin M., Springel V., White S. D. M., Jenkins A., 2010, MNRAS, 406, 896
Cooray A., Sheth R., 2002, Phys. Rep., 372, 1
Dalal N., White M., Bond J. R., Shirokov A., 2008, ApJ, 687, 12
Dawson K. S., et al., 2013, AJ, 145, 10
Foreman-Mackey D., Hogg D. W., Lang D., Goodman J., 2013, PASP, 125, 306
Foreman-Mackey D., et al., 2016, corner.py: corner.py v1.0.2, doi:10.5281/zenodo.45906, http://dx.doi.org/10.5281/zenodo.45906
Gao L., Springel V., White S. D. M., 2005, MNRAS, 363, L66
Hartlap J., Simon P., Schneider P., 2007, A&A, 464, 399
Hayashi E., White S. D. M., 2008, MNRAS, 388, 2
Holder G., 2006, ArXiv Astrophysics e-prints,
Hu W., Cohn J. D., 2006, Phys. Rev. D, 73, 067301
Huterer D., et al., 2013, preprint, (arXiv:1309.5385)
Jarvis M., Bernstein G., Jain B., 2004, MNRAS, 352, 338
Jing Y. P., Zhang P., Lin W. P., Gao L., Springel V., 2006, ApJ, 640, L119
Jing Y. P., Suto Y., Mo H. J., 2007, ApJ, 657, 664
Landy S. D., Szalay A. S., 1993, ApJ, 412, 64
Lewis A., Challinor A., Lasenby A., 2000, Astrophys. J., 538, 473
Lima M., Hu W., 2004, Phys. Rev. D, 70, 043504
Limber D. N., 1953, ApJ, 117, 134
Majumdar S., Mohr J. J., 2003, ApJ, 585, 603
Mantz A. B., et al., 2015, MNRAS, 446, 2205
Mao Y.-Y., Williamson M., Wechsler R. H., 2015, ApJ, 810, 21
Miyatake H., More S., Takada M., Spergel D. N., Mandelbaum R., Rykoff E. S., Rozo E., 2015, preprint, (arXiv:1506.06135)
More S., et al., 2016a, preprint, (arXiv:1601.06063)
More S., et al., 2016b, preprint, (arXiv:1601.06063)
Norberg P., Baugh C. M., Gaztañaga E., Croton D. J., 2009, MNRAS, 396, 19
Planck Collaboration et al., 2015b, preprint, (arXiv:1502.01589)
Planck Collaboration et al., 2015a, preprint, (arXiv:1502.01597)
Planck Collaboration et al., 2015c, preprint, (arXiv:1502.01598)
Rozo E., Rykoff E. S., 2014, ApJ, 783, 80
Rozo E., et al., 2010, ApJ, 708, 645
Rozo E., Rykoff E. S., Bartlett J. G., Evrard A., 2014, MNRAS, 438, 49
Rozo E., et al., 2015, MNRAS, 450, 592
Rykoff E. S., et al., 2014, ApJ, 785, 104
Schlegel D. J., Finkbeiner D. P., Davis M., 1998, ApJ, 500, 525
Sehgal N., et al., 2011, ApJ, 732, 44
Sereno M., Ettori S., 2015, MNRAS, 450, 3633
Simet M., McClintock T., Mandelbaum R., Rozo E., Rykoff E., Sheldon E., Wechsler R. H., 2016, preprint, (arXiv:1603.06953)
Smith R. E., et al., 2003, MNRAS, 341, 1311
Springel V., 2005, MNRAS, 364, 1105
Takahashi R., Sato M., Nishimichi T., Taruya A., Oguri M., 2012, ApJ, 761, 152
Tinker J. L., Robertson B. E., Kravtsov A. V., Klypin A., Warren M. S., Yepes G., Gottlöber S., 2010, ApJ, 724, 878
Tojeiro R., et al., 2014, MNRAS, 440, 2222
Vikhlinin A., et al., 2009, ApJ, 692, 1060
Wechsler R. H., Zentner A. R., Bullock J. S., Kravtsov A. V., Allgood B., 2006, ApJ, 652, 71
Weinberg D. H., et al., 2013, Physics Reports, 530, 87
Wu H.-Y., Rozo E., Wechsler R. H., 2008, ApJ, 688, 729
York D. G., et al., 2000, AJ, 120, 1579
Zentner A. R., Berlind A. A., Bullock J. S., Kravtsov A. V., Wechsler R. H., 2005, ApJ, 624, 505
Zu Y., et al., 2012, ArXiv: 1207.3794,
Zuntz J., et al., 2015, Astronomy and Computing, 12, 45
van Daalen M. P., Schaye J., Booth C. M., Dalla Vecchia C., 2011, MNRAS, 415, 3649

APPENDIX A: MEASUREMENTS AND BEST FIT MODELS

Figures A1 and A2 shows the angular correlation function for redMaPPer clusters for two different redshift bins, and our best fit model both when adopting a free bias parameter for each richness bin (red) and when modeling the mass–richness relation (green).

This paper has been typeset from a TEX/LATEX file prepared by the author.

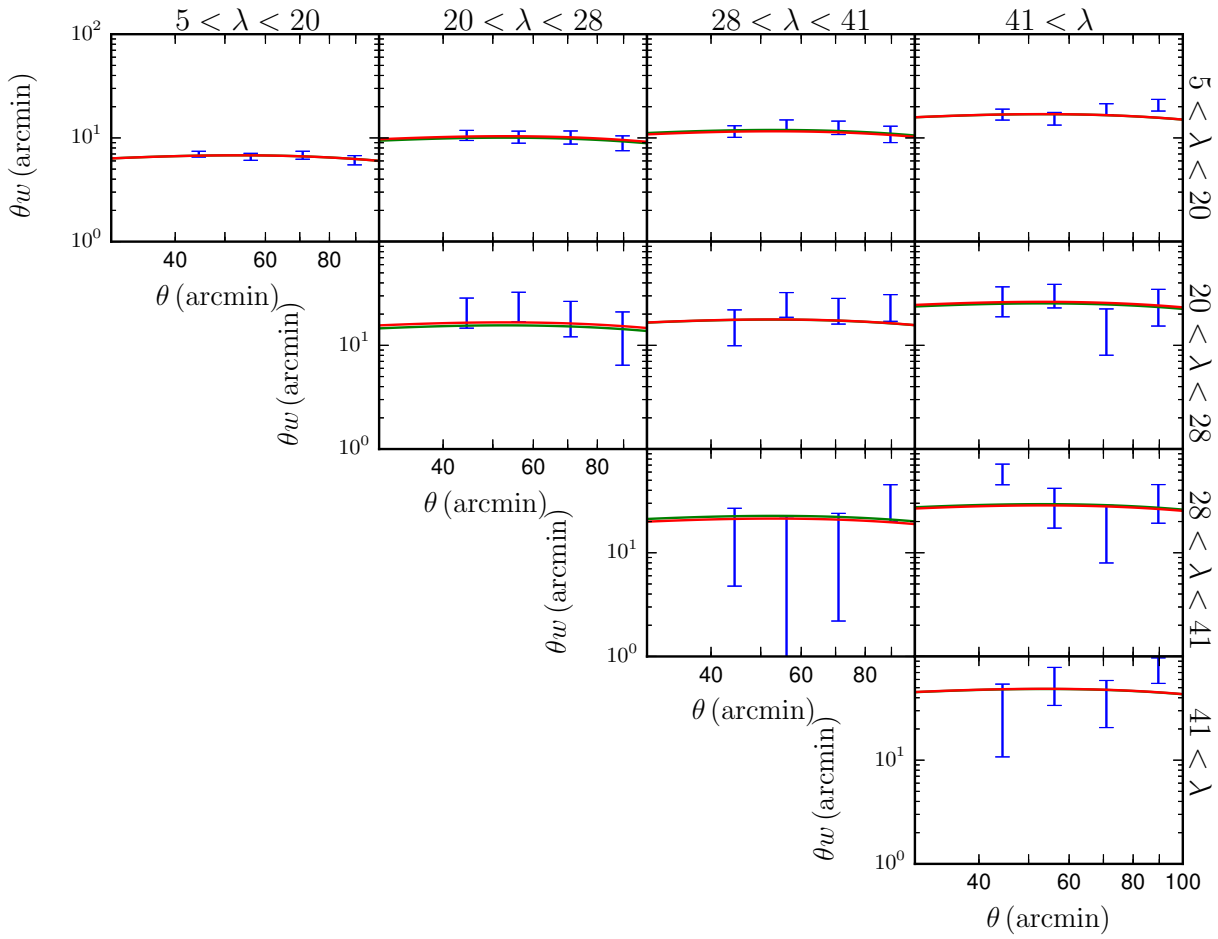

Figure A1. The angular cross-correlation function, $\theta w^{\alpha\beta}(\theta)$ between redMaPPer clusters in several different richnesses bins for the redshift interval $0.18 < z < 0.26$. The richness bins are indicated on the top and right sides of the figure. Error bars are the diagonal elements of the covariance matrix. The red curves shows the best-fitting model when each richness bin is assigned a free bias parameter, while the green curves are obtained through modeling of the mass–richness relation (in many cases, the green and red curves are indistinguishable).

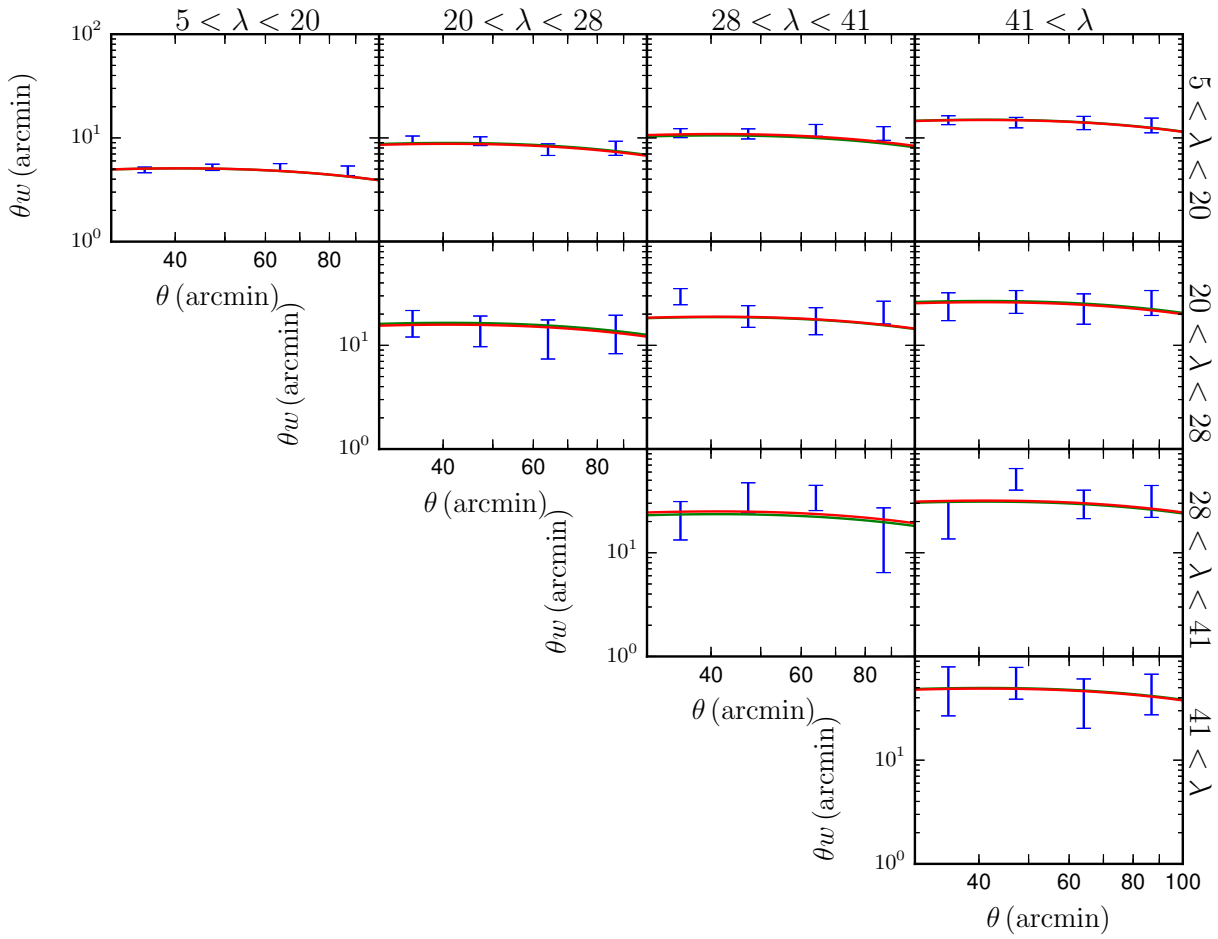

Figure A2. Same as Fig. A1, but for redMaPPer clusters with $0.26 < z < 0.33$.